Article **Open Access**

Ultra-compact lithium niobate photonic chip for high-capacity and energy-efficient wavelength-division-multiplexing transmitters

Hongxuan Liu[1], Bingcheng Pan[1], Yishu Huang[1], Jianghao He[1], Ming Zhang[1,2], Zejie Yu[1,3,4], Liu Liu[1,3,4], Yaocheng Shi[1,2,3,4] and Daoxin Dai[1,2,3,4,*]

Abstract

Recently, high-performance thin-film lithium niobate optical modulators have emerged that, together with advanced multiplexing technologies, are highly expected to satisfy the ever-growing demand for high-capacity optical interconnects utilizing multiple channels. Accordingly, in this study, a compact lithium-niobate-on-insulator (LNOI) photonic chip was adopted to establish four-channel wavelength-division-multiplexing (WDM) transmitters, comprising four optical modulators based on ultracompact 2×2 Fabry-Perot cavities and a four-channel WDM filter based on multimode waveguide gratings. The fabricated chip with four wavelength channels has a total footprint as compact as $0.3 \times 2.8 \ mm^2$, and exhibits an excess loss of ~0.8 dB as well as low inter-channel crosstalk of < -22 dB. Using this LNOI photonic chip, high-capacity data transmissions of 320 Gbps (4×80 Gbps) on-off-keying signals and 400 Gbps (4×100 Gbps) four-level pulse amplitude signals were successfully realized with the ultra-low power consumption of 11.9 fJ/bit.

Keywords: Lithium niobate on insulator, Fabry-Perot cavity, Electro-optic, Transmitter, Wavelength-division multiplexing

Introduction

With the rapid growth in use of data in artificial intelligence, 5G systems, cloud computation, and the Internet of Things, transmitters with extremely high capacities are required for data communication[1–3]. Ultrafast optical modulation is an important technology for high-capacity transmitters. In recent years, high-speed optical modulators have attracted considerable interest, and significant progress has been achieved using different mechanisms in various material systems[4–16]. Among them, optical modulators on a lithium-niobate-on-insulator (LNOI) platform have exhibited great potential, because of a linear electro-optic (EO) effect, low excess loss, and high stability[17]. In particular, LNOI EO modulators based on Mach-Zehnder interferometers and microresonators have performed excellently. For LNOI Mach-Zehnder modulators (MZMs)[18–23], the length of the phase-shifting arms is typically several millimeters, or even centimeters, to realize a low voltage. Accordingly, traveling-wave

Correspondence: Daoxin Dai (dxdai@zju.edu.cn)
[1]State Key Laboratory for Modern Optical Instrumentation, Center for Optical & Electromagnetic Research, College of Optical Science and Engineering, International Research Center for Advanced Photonics, Zhejiang University, Zijingang Campus, Hangzhou 310058, China
[2]Ningbo Research Institute, Zhejiang University, Ningbo 315100, China
Full list of author information is available at the end of the article.
These authors contributed equally: Hongxuan Liu, Bingcheng Pan

electrodes have been introduced, along with high-speed MZMs with > 100 Gbps on-off keying (OOK) modulation[22] and > 96 GBaud 16-QAM modulation[23]. However, due to their large footprint, arraying of LNOI MZMs is inconvenient for high-capacity multiplexed systems with multiple channels. In contrast, the resonator-based modulators of LNOI can be compact, which may reduce power consumption[24–27]. Meanwhile, it is possible to achieve a high modulation bandwidth by lowering the Q-factor to reduce the photon lifetime. Therefore, resonator-based LNOI modulators have attracted significant attention in recent years. In particular, we successfully demonstrated high-speed LNOI modulators based on a specific 2×2 Fabry-Perot (FP) cavity, enabling an ultra-high 3-dB bandwidth beyond 110 GHz and data capacity up to 140 Gbps[28]. More importantly, the footprint of the modulation section is as short as ~50 μm (much smaller than that of the reported LNOI ring resonator modulators[24]), which is very attractive for arraying wavelength-division multiplexing (WDM) systems.

Advanced multiplexing techniques have been widely studied to expand link capacity by transmitting data through multiple channels in parallel. In particular, WDM, in which multiple wavelength channels are introduced, has been successfully applied in recent decades. WDM filters play a key role in (de)multiplexing wavelength channels in corresponding systems[29–31]. For example, various waveguide structures have been developed in recent years to realize WDM filters with excellent performance, including arrayed-waveguide gratings (AWGs)[32,33], ring resonators[34–36], (cascaded) MZIs[37,38], and waveguide Bragg gratings[39–41]. For these WDM filters, high-quality fabrication is critical for achieving low-loss and low-phase-error light propagation in optical waveguides. Currently, several typical fabrication technologies have been established for LNOI photonic waveguides, including chemical mechanical polishing[42,43], wet etching[44], and dry etching[45,46]. Among these, the dry-etching method is typically preferred because of its process compatibility and fabrication repeatability. Further, inductively coupled plasma (ICP) etching with Ar gas is one of the most common methods for fabricating LNOI photonic waveguides and devices.

However, for X-cut LNOI photonic waveguides (which are the most popular for optical modulation), non-negligible mode hybridization might exist in sharp waveguide bends[47] or adiabatic waveguide tapers owing to the LN anisotropy and angled waveguide sidewalls. Thus, mode manipulation is challenging when light propagates through X-cut LNOI photonic integrated circuits (PICs). Furthermore, design of devices with LN anisotropy is inconvenient because accurate calculation of the accumulated phase delay is difficult in waveguide bends (which is usually indispensable in various PICs). Consequently, realizing compact and high-performance LNOI photonic devices, including WDM filters, remains complicated. For example, AWGs based on X-cut LNOI waveguides have not yet been reported because the structural design is quite complex owing to the anisotropy of the waveguide bends and free-propagation regions.

Nevertheless, great efforts have been made and impressive progress has been achieved utilizing smart designs without any waveguide bends in the key regions. For example, a four-channel coarse WDM transmitter chip on LNOI has been demonstrated utilizing a multiplexer including an angled multimode interferometer[48], which is as long as nearly two millimeters and is unsuitable for cases with many channels and narrow channel spacing. In addition, the spectral responses are not flat-top; thus, the 1-dB bandwidth is relatively small. As an alternative, in our previous work, we proposed and developed an LNOI photonic silicon filter based on a straight multimode waveguide grating (MWG)[49] that enables a box-like spectral response, and whose central wavelength and bandwidth can be designed flexibly[50].

In this study, a four-channel WDM filter with box-like responses was established using cascaded LNOI MWGs for the *first* time. For example, four channels were included and the channel spacing was set to 20 nm. In addition, the four-channel WDM filter is integrated with a 1×4 array of FP-cavity modulators, which have a particularly ultra-short modulation region of ~100 μm. The introduction of the FP-cavity modulators enables energy-efficient and high-speed optical modulation. The proposed LNOI photonic chip, which has a total footprint as small as 0.3×2.8 mm^2, can be used to realize four-channel WDM transmitters. Photonic waveguides and circuits of large scale present increased manufacturing requirements. With the advanced Ar ion etching process developed by ourselves, the chip features transport cascading and channel uniformity. Experimentally, the proposed chip enables high-capacity data transmission of 320 Gbps (4×80 Gbps) OOK signals and 400 Gbps (4×100 Gbps) PAM4 signals with the low power consumption of 11.9 fJ/bit. This indicates great potential for the large-scale photonic integration of LN, and the bright prospect of LNOI regarding its widespread use in integrated photonic devices.
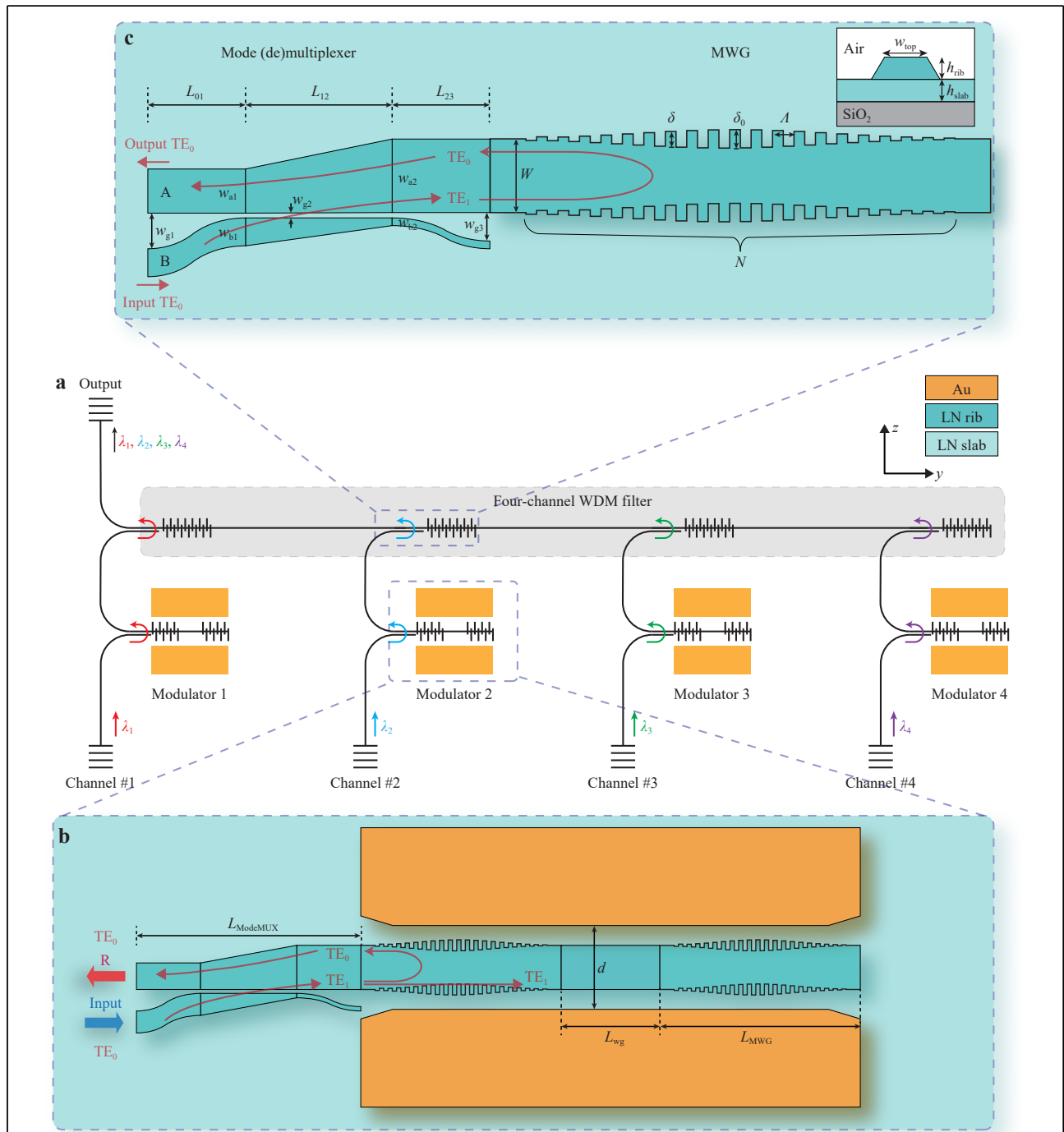
Results

Structure of lithium niobate (LN) photonic chip

Fig. 1a presents the configuration of the proposed LNOI

photonic chip for four-channel WDM transmitters comprising four FP-cavity LNOI modulators, used to modulate light of different wavelengths accordingly (Fig. 1b). The modulated signals were then multiplexed using a four-channel WDM filter based on MWGs in a cascade (Fig. 1c).

Each MWG filter comprised a mode (de)multiplexer based on an adiabatic dual-core taper (with waveguides A and B) and an MWG, as shown in Fig. 1c. The inset depicts the cross section of the LNOI ridge waveguide with

**Fig. 1 a** Schematic of configuration of the proposed lithium-niobate-on-insulator (LNOI) photonic chip for four-channel wavelength-division-multiplexing (WDM) transmitters, comprising four FP-cavity LNOI modulators. **b** 2 × 2 FP-cavity optical modulator. **c** Stage of the WDM filter, constituting a mode (de)multiplexer and a multimode waveguide grating (MWG). Inset: cross section of an LNOI ridge waveguide.

the sidewall angle of 30° (relative to the vertical axis). Here, we used a 400-nm-thick X-cut LNOI wafer, and the LNOI ridge waveguide had the etching depth of 200 nm and air up-cladding. As shown in Fig. 1c, the TE_0 mode launched from the left port of waveguide B is converted to the forward TE_1 mode at the right end of waveguide A through the mode (de)multiplexer based on the adiabatic dual-core taper. The forward TE_1 mode is then converted very efficiently to the backward TE_0 mode by the MWG when the wavelength satisfies the Bragg grating condition. One should note that the TE_1-TE_0 conversion is very efficient while the TE_1-TE_1 reflection is negligible for the MWG. Then, the backward TE_0 mode is output with very low losses from the left port of waveguide A, realized with the mode (de)multiplexer.

The mode (de)multiplexer was designed according to the method described in a previous work[51]. The core widths at the input/output ends of waveguides A and B were chosen as $(w_{a1}, w_{a2}) = (1, 2)$ μm, $(w_{b1}, w_{b2}) = (0.6, 0.2)$ μm, the taper lengths $(L_{01}, L_{12}, L_{23}) = (50, 100, 50)$ μm, and the gap widths $(w_{g1}, w_{g2}, w_{g3}) = (2, 0.25, 1.25)$ μm. The eigenmode expansion method was employed for simulating the designed mode (de)multiplexer when light is launched at the right side of waveguide A, as shown in Fig. 2a, b. The backward TE_0 mode propagates along waveguide A while the backward TE_1 mode is converted into the TE_0 mode of waveguide B. The mode (de)multiplexer has a low excess loss of ~0.05 dB and crosstalk of < −20 dB, indicating that the reflection back to the input port of waveguide B is very low. Longer adiabatic tapers can achieve lower losses and lower crosstalk, at the expense of larger size.

The MWG has the effective waveguide width W of 2 μm, and Gaussian apodization is applied to the corrugation depth δ to realize a high sidelobe-suppression ratio (SLSR) and reduce the crosstalk between channels. Accordingly, $\delta = \delta_0 \exp[-b(i-N/2)^2/N^2]$, where δ_0 is the maximum corrugation depth, b is the apodization index, N is the total number of the grating period, and $i = 1, \ldots, N$. Here, the apodization index b was set to 10. The reflectivity and the bandwidth of MWG filters are mainly
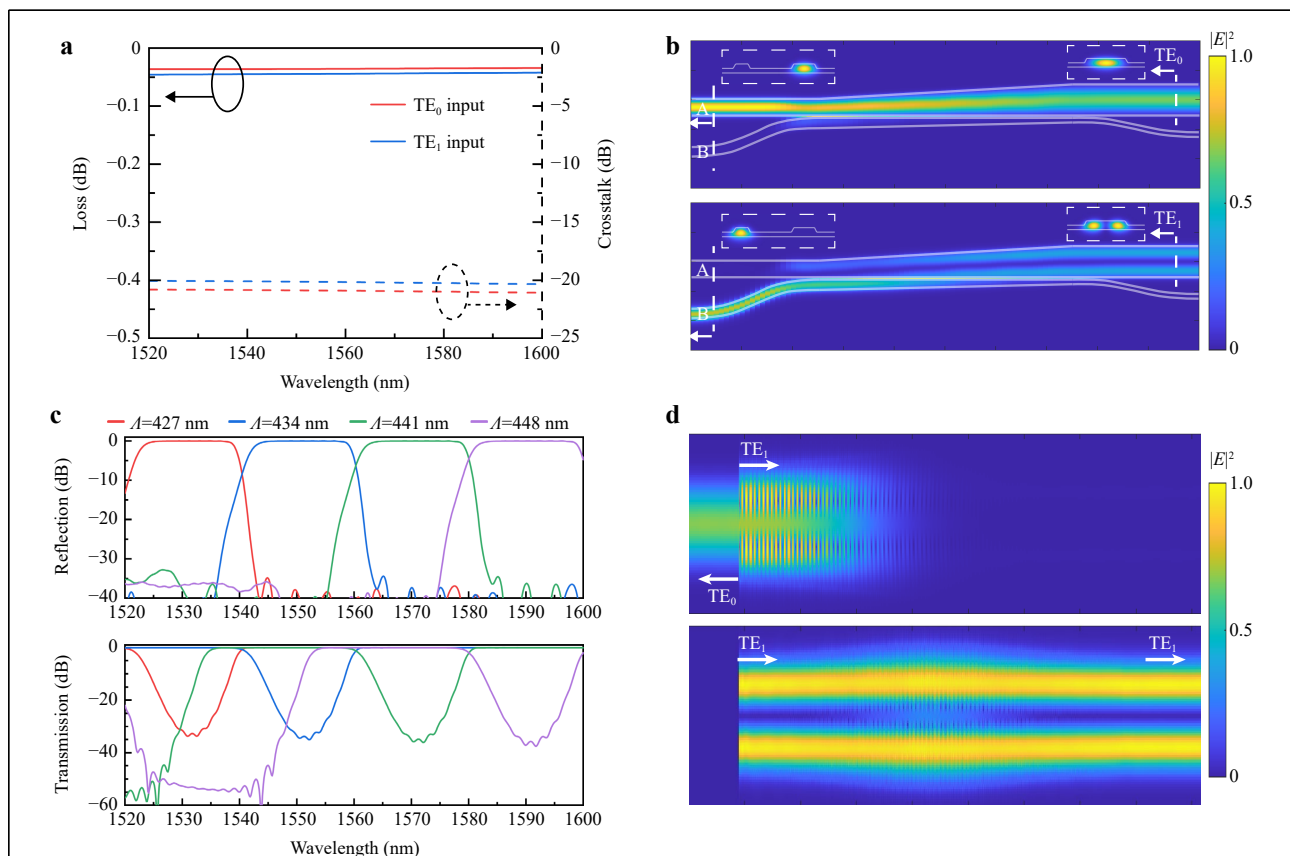
Fig. 2 Calculated results for the dual-core mode (de)multiplexer **a**, **b** and MWGs for the WDM filter **c** and **d**. **a** Propagation loss and crosstalk of the mode (de)multiplexer. **b** Light propagation in a mode (de)multiplexer when the backward TE_0 or TE_1 mode is launched at the right port of waveguide A. Insets: eigenmodes at different cross sections. **c** TE_1-TE_0 reflection and TE_1-TE_1 transmission of the four MWGs with different grating period Λ. **d** Simulated light propagation in the MWG for channel #2 at wavelengths of 1551 nm (reflection) and 1571 nm (transmission).

determined by N and δ, which are optimized to be 450 and 640 nm, respectively. The MWG periods Λ of the four channels were chosen as 427, 434, 441, and 448 nm according to the central wavelength requirements.

Fig. 2c, d shows the three-dimensional finite-difference time-domain (3D-FDTD) simulation results of the TE_1-TE_0 reflection (i.e., the mode conversion from the forward TE_1 to the backward TE_0 mode) and the forward transmission of the TE_1 mode for the four designed MWGs individually when the TE_1 mode is launched (forward). The corresponding central wavelengths of the four MWG filters are 1531, 1551, 1571, and 1591 nm. It can be seen that the TE_1-TE_0 reflectivity of the MWG is as high as 99.5% and finally the backward TE_0 mode is then output with very low losses from waveguide A of the mode (de)multiplexer. Correspondingly the power coupled from the backward TE_0 mode back to the input port (waveguide B) is negligible because the mode (de)multiplexer works well with very low crosstalk. In addition, the MWG reflection from the forward TE_1 mode to the backward TE_1 mode is less than −50 dB, as expected in theory, and thus little power is reflected back to the input port (waveguide B).

Fig. 2c shows that the 1-dB bandwidth is as large as 16.5 nm (which is very high with respect to the channel spacing of 20 nm), featuring low-loss box-like responses. Furthermore, the SLSR is theoretically better than 35 dB over a wide wavelength range. In the wavelength range shorter than the Bragg wavelength of the desired TE_1-TE_0 reflection, the TE_1 mode can partially be coupled/reflected into the higher-order modes with lower effective indices, according to the coupled mode theory. For example, TE_1-TE_2 reflection occurs in the range of 1525–1545 nm for the MWG of channel #4, as exhibited in the transmission spectrum in Fig. 2c (purple line). Fortunately, the reflected higher-order mode is not supported in the following part and dissipates along the tapers and the mode (de)multiplexers, which thus has no effect on the channels at the left. The similar situation occurs when the TE_0 mode is launched to the MWG. To ensure that the output TE_0 mode of each channel passes through subsequent filters with low loss, the four MWGs are cascaded in an optimal sequence so that $\lambda_1 < \lambda_2 < \lambda_3 < \lambda_4$, where λ_1 and λ_4 are respectively the central wavelengths of the MWGs at the leftmost and the rightmost, as depicted in Fig. 1a. Fig. 2d presents the simulated light propagation of the input TE_1 mode in the designed MWG with $\Lambda = 434$ nm (channel #2) when operated at wavelengths of 1551 and 1571 nm, respectively.
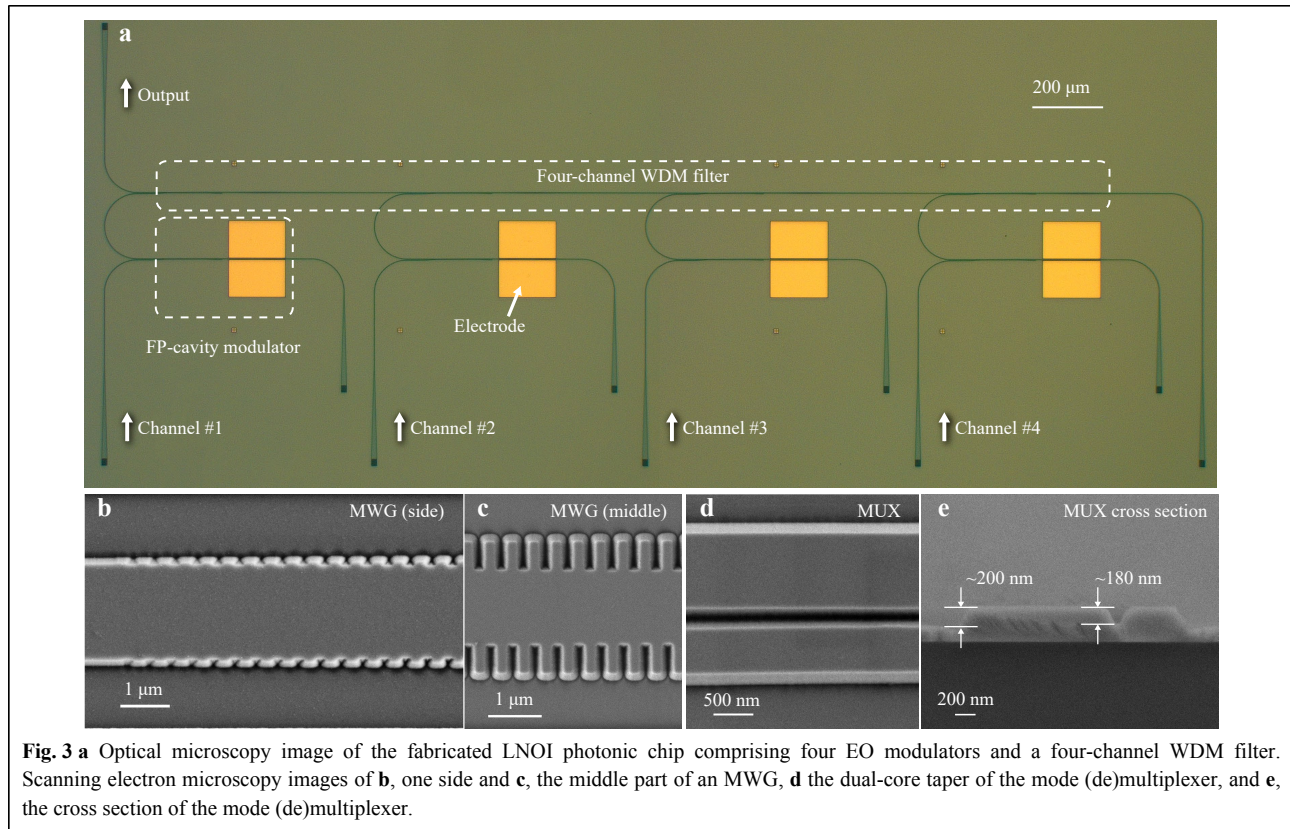
For the modulator based on a 2×2 FP cavity, as shown in Fig. 1b, a pair of MWGs is used as the input and output reflectors. A mode (de)multiplexer was incorporated to separate the light reflected from the FP cavity from the incident light. The G-S electrodes with separation d were placed symmetrically on both sides of the FP cavity. The refractive index of the LN is modulated by the Pockels effect when electrical signals are applied to the electrodes. Accordingly, resonance wavelength shifts and intensity modulation were achieved at the reflection port for lunched light with a fixed wavelength. Based on our previous work, the balance between the modulation bandwidth and efficiency for an FP-cavity modulator can be achieved by carefully designing the reflectivity of the MWGs and the cavity length. To avoid the metal absorption loss in the MWG area, $\delta_0 = 600$ nm and $d = 5$ μm were selected for the FP cavity. In theory, when the period number N for the MWG is set to 180, the estimated reflectivity is 0.85 and intrinsic grating loss is lower than 0.015 dB; Theoretically, the loss can be reduced by decreasing the corrugation depth and increasing the period number[52,53]. The length L_{wg} was set to 20 μm to form a ~100-μm-long equivalent modulation region.

Characterization of fabricated devices

The designed LNOI photonic chip constituting four-channel EO modulators was fabricated on an X-cut LNOI wafer (*NANOLN*) with a 400-nm-thick $LiNbO_3$ layer and a 3-μm-thick buried oxide layer. Further details regarding the fabrication can be found in **Materials and Methods**. Fig. 3a displays an optical microscopy image of the fabricated LNOI photonic chip with four FP-cavity modulators and a four-channel WDM filter. Fig. 3b–e presents the scanning electron microscopy images for different apodization parts of the MWG, as well as the dual-core waveguide coupling region for the mode (de)multiplexer and its cross section, respectively. It is clear that the waveguide sidewalls were all smooth with the same angle. As shown in Fig. 3e, the etch depth of the 250-nm-width trench is approximately 180 nm, shallower than other open regions (with an etch depth of ~200 nm). This is because smaller feature size leads to a slower etch rate, which is the so-called lag effect[54], existing commonly in the dry etching process for narrow trenches. The lag effect usually occurs with high aspect ratio (> 1) in other platforms such as silicon. In contrast, it should be noted that the aspect ratio is 0.8 only (< 1.0) in our experiment. This is probably because of the non-vertical sidewall (~30° relative to the vertical axis) of the LN waveguide. Thus, such a lag effect should be carefully considered for the device design.

The fabricated LNOI photonic chip was characterized using a setup including a broadband-amplified spontaneous-emission (ASE) light source and an optical

Fig. 3 a Optical microscopy image of the fabricated LNOI photonic chip comprising four EO modulators and a four-channel WDM filter. Scanning electron microscopy images of **b**, one side and **c**, the middle part of an MWG, **d** the dual-core taper of the mode (de)multiplexer, and **e**, the cross section of the mode (de)multiplexer.

spectrum analyzer (OSA). Fig. 4a presents the measured output spectra of the four-channel MWG-based WDM filter. The results were normalized to the transmission of a straight waveguide connected to two grating couplers on the same chip. For the fabricated WDM filter, the channel spacing is 20 nm (which agrees well with the design value), while the excess loss is < 0.8 dB and the channel crosstalk is less than –22 dB at the central wavelengths. More importantly, the WDM filter features box-like responses with a 1-dB bandwidth as large as 16 nm. Some ripples were observed at the edges of the channels. No ripples are observed from the simulation result (Fig. 2c) or the measurement transmission of a single MWG, indicating that ripples originated from the interference due to the reflections of the cascaded MWGs. Fortunately, these ripples do not have a notable negative impact on devices used in WDM systems. Fig. 4b exhibits the measured transmissions from the four input ports to the output port of the fabricated LNOI photonic chip. The measured transmissions were a combination of the transmissions of the FP-cavity modulator and MWG-based WDM filter. Consequently, several notches corresponded to the FP cavity resonance wavelengths, as observed from the measured transmission for each channel. The Q-factors of the FP cavities for four channels are approximately 5450,

Fig. 4 a Measured transmissions of the fabricated four-channel WDM filter based on MWGs. **b** Measured transmissions from one of the four input ports to the output port of the fabricated LNOI photonic chip.
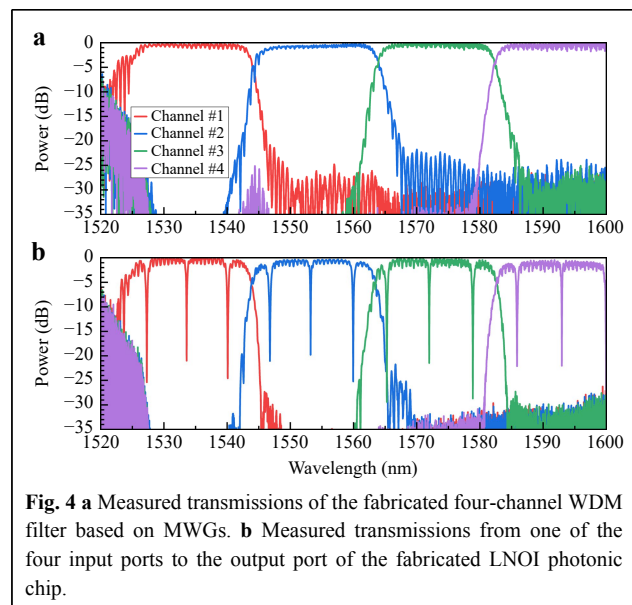
6160, 6180 and 6450, the extinction ratios (ERs) are all greater than 20 dB, and the FSR of each cavity is approximately 7 nm, which is consistent with the design. Note that the cavity FSR can be increased, such as by decreasing the FP cavity length L_{wg}, or introducing a defect in the MWG to form a phase-shifted grating[55]. From

Fig. 4b, the excess losses of Channels #1 and #4 are 0.4 and 0.8 dB respectively, indicating that the present WDM filter has an additional loss of ~0.15 dB per stage, and thus is possible to be scaled for more channels in the future. To demonstrate the EO property, a static electric field was applied to the modulators. From the measured resonance shift on voltage, a tuning slope of 9.6 pm/V could be obtained.

Experiments of data transmissions

The fabricated LNOI photonic chip was characterized for high-speed data transmission. Further details regarding the experimental setup can be found in **Materials and Methods**. The modulation bandwidth limited by the photon lifetime in theory can be estimated as BW = f_0/Q, where f_0 is the resonant frequency and Q is the quality factor of a cavity. For the modulators of the four channels, the bandwidths are approximately 36, 31, 31, and 29 GHz, respectively, according to their measured Q factors. Adjusting the operation wavelength detuning to the resonance is helpful to further improve the 3-dB modulation bandwidth, as analyzed in our previous work[28]. Fig. 5 shows the measured eye diagrams for the four channels with 40/80 Gbps OOK signals and the 100 Gbps (50 GBaud) PAM4 signals. Limited by laboratory facilities, the experiments of data transmissions were run for each channel individually. As shown in Fig. 5a–d, all the channels perform similarly for the 40-Gbps OOK signals, featuring the dynamic ERs of 2.99, 3.11, 2.96, and 3.12 dB, respectively. For the eye diagrams of these four channels, there are slight differences due to the inconsistency of their optimal operating biases in the

testing. The measured results for the 80-Gbps OOK signals are displayed in Fig. 5e–h. Owing to the limitations of the bandwidth and linear range of the radiofrequency (RF) amplifier, the voltage V_{pp} applied to the probe drops to 1.5 V and consequently, the signal is distorted. Meanwhile, the other electronic components such as the RF cables also greatly limit the experimental measurement of high-speed transmissions. By increasing the drive voltage and improving the bandwidth of the measurement system, high-quality OOK eye diagrams can be achieved at very high data rates. Alternatively, Fig. 5i–l presents the measured eye diagrams for the 100 Gbps PAM4 signals. The eyes are open for three channels (#1–#3), while the eye diagram for channel #4 is worse. This is owing to the low coupling efficiency of the grating couplers and the low gain coefficient of the erbium-doped fiber amplifier when operating at a long wavelength of approximately 1600 nm. Fortunately, broadband fiber-chip couplers (e.g., edge coupling[56,57]) for LNOI waveguides are available using the present fabrication technology. Consequently, the present transmitters are expected to work well with all four channels and enable a high total capacity of 4 × 100 Gbps. For each FP-cavity modulator in the present photonic chip, the capacitance is approximately 21.1 fF and the corresponding electrical energy consumption is estimated to be ~11.9 fJ/bit for the data transmitting up to 80 Gbps and beyond when operating with the bias of 1.5 V_{pp}. The link capacity can be further improved by introducing additional wavelength channels.

Discussion

We proposed and demonstrated an ultracompact LNOI
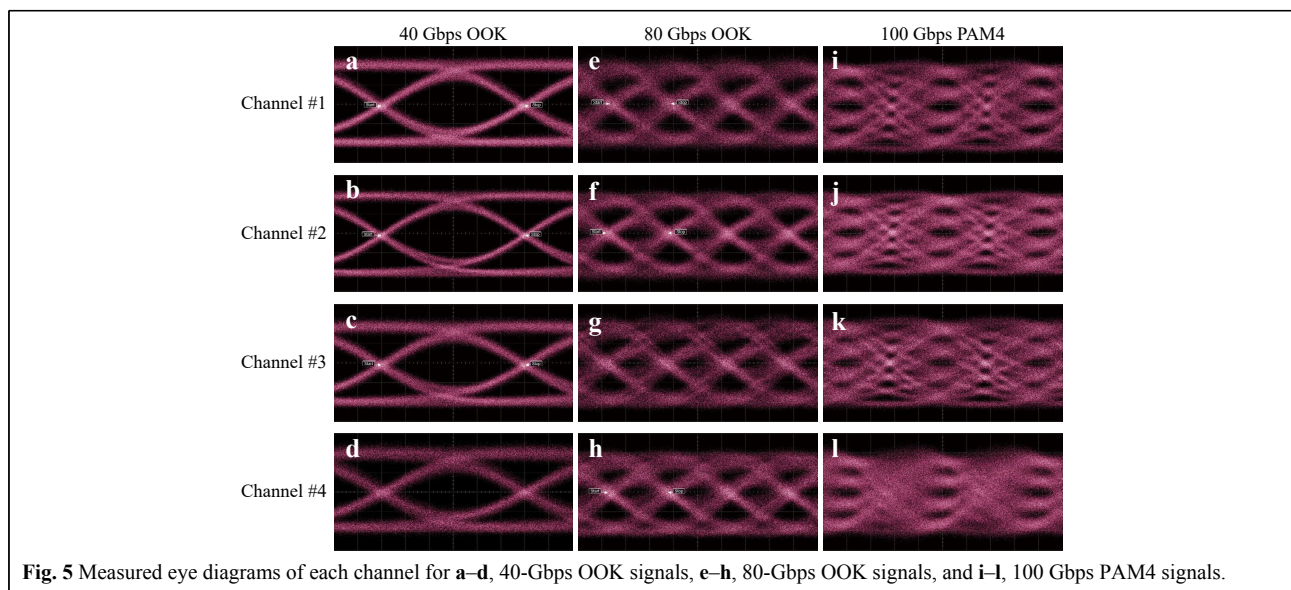
Fig. 5 Measured eye diagrams of each channel for **a–d**, 40-Gbps OOK signals, **e–h**, 80-Gbps OOK signals, and **i–l**, 100 Gbps PAM4 signals.

photonic chip to realize four-channel WDM transmitters by monolithically integrating four FP-cavity modulators and a four-channel WDM filter based on MWGs. The designed and fabricated WDM filters exhibited box-like responses with low excess losses (< 0.8 dB) and low crosstalk (better than −22 dB) for all channels. For the fabricated FP-cavity modulator of each channel, which had a Q-factor of approximately 6000, the extinction ratio was greater than 20 dB and the FSR was approximately 7 nm. All four channels demonstrated very low and uniform excess losses. The present photonic chip integrating four FP-cavity modulators and a four-channel WDM filter has a very compact footprint of 0.3×2.8 mm^2, which is attractive for cases requiring even more WDM channels. The present LNOI photonic chip was further employed to realize high-capacity data transmission, and eye diagrams were demonstrated with 320-Gbps (4 × 80 Gbps) OOK signals and 400-Gbps (4 × 100 Gbps) PAM4-signals. Correspondingly, the power consumption is as low as 11.9 fJ/bit for each channel. The present photonic chip with an ultracompact footprint can be scaled for more channels and thus shows great potential for further realization of ultrahigh-capacity and energy-efficient WDM transmitters on LNOI in the future. In addition, the fabrication process can be improved by introducing SiO_2[58], amorphous-Si[59], or Cr[60,61] hard masks. With an improved etching process, the propagation loss (mainly originating from the scattering loss at the sidewalls) can be reduced to a wafer scale[58], which is very helpful for developing high-performance LNOI photonic integrated circuits and satisfying the growing demands for various applications.

Materials and methods

Fabrication

Note that the popular fluorine-based reactive-ion etching method used for silicon or silicon nitride is not available for LN because of the redeposition of the solid byproduct lithium fluorine, which impedes further etching and increases the sidewall roughness. Instead, a popular approach for LN dry etching involves the use of Ar gas. For such a pure physical etching process, the challenge is to realize vertical and smooth sidewalls using an etching recipe with high selectivity. Therefore, etching parameters should be carefully optimized. In the etching process, Ar plasma may damage the mask and roughen the sidewalls, particularly in the deep-etching case. Fortunately, the etching selectivity can be improved by decreasing the power and gas flow rate[45] when using electron beam resists such as HSQ[14,46], ZEP[25], and ma-N2403[22,27] for the mask.

The fabrication of the LNOI photonic device is described in detail as follows. First, the waveguide structure patterns were defined via a single step of electron-beam lithography (EBL) in a maN-2403 resist with a thickness of approximately 350 nm. Second, the LN layer was etched with the depth of 200 nm through an optimized Ar-gas-based ICP process with an etch rate of ~30 nm/min. Cleaning of the chamber before etching is usually necessary. During the etching process, the chamber temperature continually rises. To avoid the mask being damaged by high temperature and ensure selectivity in this study, the temperature was set to 10 °C and He gas was fed under the sample for cooling. Finally, titanium/gold electrodes with thicknesses of 10/150 nm were deposited via a liftoff process.

Experimental setup

In the high-speed data transmission experiment, a pseudo-random binary sequence electrical signal was generated using an arbitrary waveform generator connected to a clock source. The driver signal was fed to a linear RF amplifier (SHF S807 C) followed by a 6-dB attenuator to avoid reflection damage before being coupled to the GS pads via a 67-GHz RF probe. The actual peak-to-peak V_{pp} applied to the probe was approximately 1.8 V at the 40-Gbps data rate of the OOK signals. A tunable continuous-wave (CW) laser source near the resonant wavelength was fed into the input port of the corresponding channel. The modulated light was then multiplexed to the output port using a WDM filter. Finally, the transmitted signal was amplified through an erbium-doped fiber amplifier comprising an optical bandpass filter and collected by an electrical sampling oscilloscope.

Author details

[1]State Key Laboratory for Modern Optical Instrumentation, Center for Optical & Electromagnetic Research, College of Optical Science and Engineering, International Research Center for Advanced Photonics, Zhejiang University, Zijingang Campus, Hangzhou 310058, China. [2]Ningbo Research Institute, Zhejiang University, Ningbo 315100, China. [3]Jiaxing Key Laboratory of Photonic Sensing & Intelligent Imaging, Jiaxing 314000, China. [4]Intelligent Optics & Photonics Research Center, Jiaxing Research Institute Zhejiang University, Jiaxing 314000, China

Author contributions

D. D. and B. P. proposed the original concept. H.L. designed and fabricated the chips. Y.H. performed LN etching. J.H. and M.Z. advised on the design of the WDM multiplexers. H.L. and B.P. performed measurements. H.L., B.P., Z.Y., and D.D. prepared the manuscript. D.D. supervised the project. All authors analyzed the experimental results and approved the final manuscript.

Conflict of interest

The authors declare no competing interests.

References

1. Zheng, K. Y. et al. Mid-infrared all-optical modulators based on an acetylene-filled hollow-core fiber. *Light:Advanced Manufacturing* **3**, 50 (2022).
2. Liang, D. & Bowers, J. E. Recent progress in heterogeneous III-V-on-silicon photonic integration. *Light:Advanced Manufacturing* **2**, 59-83 (2021).
3. Zhang, L. et al. 'Plug-and-play' plasmonic metafibers for ultrafast fibre lasers. *Light: Advanced Manufacturing* **3**, 45 (2022).
4. Li, M. F. et al. Silicon intensity Mach-Zehnder modulator for single lane 100 Gb/s applications. *Photonics Research* **6**, 109-116 (2018).
5. Zhalehpour, S. et al. System optimization of an all-silicon IQ modulator: achieving 100-gbaud dual-polarization 32QAM. *Journal of Lightwave Technology* **38**, 256-264 (2020).
6. Zhang, Y. G. et al. 240 Gb/s optical transmission based on an ultrafast silicon microring modulator. *Photonics Research* **10**, 1127-1133 (2022).
7. Hiraki, T. et al. Heterogeneously integrated III-V/Si MOS capacitor Mach–Zehnder modulator. *Nature Photonics* **11**, 482-485 (2017).
8. Li, Q. et al. Si racetrack optical modulator based on the III-V/Si hybrid MOS capacitor. *Optics Express* **29**, 6824-6833 (2021).
9. Haffner, C. et al. Low-loss plasmon-assisted electro-optic modulator. *Nature* **556**, 483-486 (2018).
10. Heni, W. et al. Plasmonic IQ modulators with attojoule per bit electrical energy consumption. *Nature Communications* **10**, 1694 (2019).
11. Mao, J. W. et al. Efficient silicon and side-cladding waveguide modulator with electro-optic polymer. *Optics Express* **30**, 1885-1895 (2022).
12. Ummethala, S. et al. Hybrid electro-optic modulator combining silicon photonic slot waveguides with high-k radio-frequency slotlines. *Optica* **8**, 511-519 (2021).
13. Huang, Y. S. et al. High-bandwidth Si/In$_2$O$_3$ hybrid plasmonic waveguide modulator. *APL Photonics* **7**, 051301 (2022).
14. He, M. B. et al. High-performance hybrid silicon and lithium niobate Mach–Zehnder modulators for 100 Gbit s^{-1} and beyond. *Nature Photonics* **13**, 359-364 (2019).
15. Wang, C. et al. Integrated lithium niobate electro-optic modulators operating at CMOS-compatible voltages. *Nature* **562**, 101-104 (2018).
16. Sorianello, V. et al. Graphene–silicon phase modulators with gigahertz bandwidth. *Nature Photonics* **12**, 40-44 (2018).
17. Zhang, M. et al. Integrated lithium niobate electro-optic modulators: when performance meets scalability. *Optica* **8**, 652-667 (2021).
18. Xu, M. Y. et al. High-performance coherent optical modulators based on thin-film lithium niobate platform. *Nature Communications* **11**, 3911 (2020).
19. Hu, J. Y. et al. Folded thin-film lithium niobate modulator based on a poled Mach–Zehnder interferometer structure. *Optics Letters* **46**, 2940-2943 (2021).
20. Pan, B. C. et al. Demonstration of high-speed thin-film lithium-niobate-on-insulator optical modulators at the 2-µm wavelength. *Optics Express* **29**, 17710-17717 (2021).
21. Kharel, P. et al. Breaking voltage–bandwidth limits in integrated lithium niobate modulators using micro-structured electrodes. *Optica* **8**, 357-363 (2021).
22. Chen, G. X. et al. High performance thin-film lithium niobate modulator on a silicon substrate using periodic capacitively loaded traveling-wave electrode. *APL Photonics* **7**, 026103 (2022).
23. Wang, Z. et al. Silicon–lithium niobate hybrid intensity and coherent modulators using a periodic capacitively loaded traveling-wave electrode. *ACS Photonics* **9**, 2668-2675 (2022).
24. Wang, C. et al. Nanophotonic lithium niobate electro-optic modulators. *Optics Express* **26**, 1547-1555 (2018).
25. Li, M. X. et al. Lithium niobate photonic-crystal electro-optic modulator. *Nature Communications* **11**, 4123 (2020).
26. Pohl, D. et al. 100-GBd waveguide bragg grating modulator in thin-film lithium niobate. *IEEE Photonics Technology Letters* **33**, 85-88 (2021).
27. Pan, B. C. et al. Compact electro-optic modulator on lithium niobate. *Photonics Research* **10**, 697-702 (2022).
28. Pan, B. C. et al. Ultra-compact lithium niobate microcavity electro-optic modulator beyond 110 GHz. *Chip* **1**, 100029 (2022).
29. Moralis-Pegios, M. et al. 4-channel 200 Gb/s WDM O-band silicon photonic transceiver sub-assembly. *Optics Express* **28**, 5706-5714 (2020).
30. Timurdogan, E. et al. 400G silicon photonics integrated circuit transceiver chipsets for CPO, OBO, and pluggable modules. Proceedings of the Optical Fiber Communication Conference (OFC) 2020. San Diego, California, USA: Optica Publishing Group, 2020.
31. Li, C. et al. Hybrid WDM-MDM transmitter with an integrated Si modulator array and a micro-resonator comb source. *Optics Express* **29**, 39847-39858 (2021).
32. Pathak, S. et al. Comparison of AWGs and echelle gratings for wavelength division multiplexing on silicon-on-insulator. *IEEE Photonics Journal* **6**, 4900109 (2014).
33. Dai, D. X. et al. Monolithically integrated 64-channel silicon hybrid demultiplexer enabling simultaneous wavelength- and mode-division-multiplexing. *Laser & Photonics Reviews* **9**, 339-344 (2015).
34. Dahlem, M. S. et al. Reconfigurable multi-channel second-order silicon microring-resonator filterbanks for on-chip WDM systems. *Optics Express* **19**, 306-316 (2011).
35. Papaioannou, S. et al. On-chip dual-stream DWDM eight-channel-capable SOI-based MUX s/DEMUX s with 40-GH z channel bandwidth. *IEEE Photonics Journal* **7**, 7900210 (2015).
36. Liu, D. J. et al. High-order adiabatic elliptical-microring filter with an ultra-large free-spectral-range. *Journal of Lightwave Technology* **39**, 5910-5916 (2021).
37. Horst, F. et al. Cascaded Mach-Zehnder wavelength filters in silicon photonics for low loss and flat pass-band WDM (de-)multiplexing. *Optics Express* **21**, 11652-11658 (2013).
38. Xu, H. N., Dai, D. X. & Shi, Y. C. Low-crosstalk and fabrication-tolerant four-channel CWDM filter based on dispersion-engineered Mach-Zehnder interferometers. *Optics Express* **29**, 20617-20631 (2021).
39. Liu, D. J., Zhang, M. & Dai, D. X. Low-loss and low-crosstalk silicon triplexer based on cascaded multimode waveguide gratings. *Optics Letters* **44**, 1304-1307 (2019).
40. Liu, Y. et al. C-band four-channel CWDM (de-)multiplexers on a thin film lithium niobate–silicon rich nitride hybrid platform. *Optics Letters* **46**, 4726-4729 (2021).
41. Liu, D. J. et al. First demonstration of an on-chip quadplexer for passive optical network systems. *Photonics Research* **9**, 757-763 (2021).

42. Zhou, J. X. et al. Electro-optically switchable optical true delay lines of meter-scale lengths fabricated on lithium niobate on insulator using photolithography assisted chemo-mechanical etching. *Chinese Physics Letters* **37**, 084201 (2020).

43. Wu, R. B. et al. Fabrication of a multifunctional photonic integrated chip on lithium niobate on insulator using femtosecond laser-assisted chemomechanical polish. *Optics Letters* **44**, 4698-4701 (2019).

44. Hu, H. et al. Lithium niobate ridge waveguides fabricated by wet etching. *IEEE Photonics Technology Letters* **19**, 417-419 (2007).

45. Ulliac, G. et al. Argon plasma inductively coupled plasma reactive ion etching study for smooth sidewall thin film lithium niobate waveguide application. *Optical Materials* **53**, 1-5 (2016).

46. Zhang, M. et al. Monolithic ultra-high-*Q* lithium niobate microring resonator. *Optica* **4**, 1536-1537 (2017).

47. Pan, B. C. et al. Compact racetrack resonator on LiNbO₃. *Journal of Lightwave Technology* **39**, 1770-1776 (2021).

48. Chen, K. X. et al. Four-channel CWDM transmitter chip based on thin-film lithium niobate platform. *Journal of Semiconductors* **43**, 112301 (2022).

49. He, J. H. et al. High-performance lithium-niobate-on-insulator optical filter based on multimode waveguide gratings. *Optics Express* **30**, 34140-34148 (2022).

50. Liu, D. J. et al. Four-Channel CWDM (de)multiplexers using cascaded multimode waveguide gratings. *IEEE Photonics Technology Letters* **32**, 192-195 (2020).

51. Dai, D. X. et al. 10-Channel mode (de)multiplexer with dual polarizations. *Laser & Photonics Reviews* **12**, 1700109 (2018).

52. Hu, Y. W. et al. Characterization of low loss waveguides using bragg gratings. *IEEE Journal of Selected Topics in Quantum Electronics* **24**, 6101508 (2018).

53. Liu, D. J., Wu, H. & Dai, D. X. Silicon multimode waveguide grating filter at 2 µm. *Journal of Lightwave Technology* **37**, 2217-2222 (2019).

54. Gottscho, R. A., Jurgensen, C. W. & Vitkavage, D. J. Microscopic uniformity in plasma etching. *Journal of Vacuum Science & Technology B:Microelectronics and Nanometer Structures Processing, Measurement, and Phenomena* **10**, 2133-2147 (1992).

55. Shi, W. et al. Silicon photonic grating-assisted, contra-directional couplers. *Optics Express* **21**, 3633-3650 (2013).

56. Hu, C. R. et al. High-efficient coupler for thin-film lithium niobate waveguide devices. *Optics Express* **29**, 5397-5406 (2021).

57. Ying, P. et al. Low-loss edge-coupling thin-film lithium niobate modulator with an efficient phase shifter. *Optics Letters* **46**, 1478-1481 (2021).

58. Luke, K. et al. Wafer-scale low-loss lithium niobate photonic integrated circuits. *Optics Express* **28**, 24452-24458 (2020).

59. Wang, C. et al. Second harmonic generation in nano-structured thin-film lithium niobate waveguides. *Optics Express* **25**, 6963-6973 (2017).

60. Krasnokutska, I. et al. Ultra-low loss photonic circuits in lithium niobate on insulator. *Optics Express* **26**, 897-904 (2018).

61. Liu, Y. et al. Low Vπ thin-film lithium niobate modulator fabricated with photolithography. *Optics Express* **29**, 6320-6329 (2021).